

Superfluidity of a laser-stirred Bose-Einstein condensate

Hannes Kiehn,¹ Vijay Pal Singh ,^{1,2} and Ludwig Mathey^{1,3}

¹Zentrum für Optische Quantentechnologien and Institut für Laserphysik, Universität Hamburg, 22761 Hamburg, Germany

²Institut für Theoretische Physik, Leibniz Universität Hannover, Appelstraße 2, 30167 Hannover, Germany

³The Hamburg Centre for Ultrafast Imaging, Luruper Chaussee 149, Hamburg 22761, Germany



(Received 18 December 2021; accepted 23 March 2022; published 25 April 2022)

We study superfluidity of a cigar-shaped Bose-Einstein condensate by stirring it with a Gaussian potential oscillating back and forth along the axial dimension of the condensate, motivated by experiments of Raman *et al.* [*Phys. Rev. Lett.* **83**, 2502 (1999)]. Using classical-field simulations and perturbation theory, we examine the induced heating rate, based on the total energy of the system, as a function of the stirring velocity v . We identify the onset of dissipation by a sharply increasing heating rate above a velocity v_c , which we define as the critical velocity. We show that v_c is influenced by the oscillating motion, the strength of the stirrer, the temperature, and the inhomogeneous density of the cloud. This results in a vanishing v_c for the parameters similar to the experiments, which is inconsistent with the measurement of nonzero v_c . However, if the heating rate is based on the thermal fraction after a 100 ms equilibration time, our simulation recovers the experimental observations. We demonstrate that this discrepancy is due to the slow relaxation of the stirred cloud and dipole mode excitation of the cloud.

DOI: [10.1103/PhysRevA.105.043317](https://doi.org/10.1103/PhysRevA.105.043317)

I. INTRODUCTION

An intriguing phenomenon of quantum liquids is the emergence of superfluidity, which was first observed in liquid helium [1,2]. This superfluid behavior can be tested by dragging an object through a stationary fluid and examining the dissipationless flow around this object. For an object moving at a velocity v , dissipationless flow occurs below a certain critical velocity v_c . Above this velocity, dissipation occurs via the creation of excitations such as phonons and vortices. An estimate of the critical velocity is given by the Landau criterion $v_c = \min(E_k/\hbar\mathbf{k})$, where E_k is the energy of an excitation with momentum $\hbar\mathbf{k}$ [3]. This predicts the critical velocity to be the roton velocity for liquid ^4He and the pair-breaking velocity for liquid ^3He , consistent with the measurements in Refs. [4–6].

With the advent of Bose-Einstein condensates (BECs) of dilute gases, the study of superfluidity was expanded to a wide range of quantum liquids. A pioneering technique of local perturbation, namely, laser stirring, was employed for probing superfluidity in these systems. This includes the measurements of superfluidity in cigar-shaped condensates [7–10], two-dimensional condensates [11], and three-dimensional condensates [12]. Given this broad variety of systems, different origins of the onset of dissipation have been identified, such as vortex-antivortex creation [13] for the experiment in Ref. [11] and phonon creation [14] for the experiment in Ref. [12]. Vortex shedding and quantized vortices were observed in Refs. [15–21]. Other stirring experiments include those in Refs. [22–26]. Laser stirring is also employed to generate controlled vortex distributions [27–29]. A number of theoretical studies were reported in Refs. [30–40].

In Ref. [7] a cigar-shaped cloud of ^{23}Na atoms was stirred with a blue-detuned laser beam oscillating back and forth in the axial direction. Using a strong beam, the superfluid response was measured based on the thermal fraction determined as a function of the stirring velocity, which is varied by the stirring displacement at a fixed stirring frequency. The resulting critical velocity was $v_c/v_B = 0.25$, where v_B is the Bogoliubov phonon velocity. In follow-up experiments with improved calorimetry [8], the critical velocity was determined using low stirring velocities and for a colder system, yielding $v_c/v_B = 0.07 \pm 0.01$.

In this paper we study the experiments of Ref. [7] from a theoretical perspective. The stirring process is described in Fig. 1(a), where the stirring velocity is determined by $v = 4fd$, with f the frequency and d the displacement. This back-and-forth oscillating motion is qualitatively distinct from a circular stirring motion [14] and dramatically affects the onset of dissipation, as we describe in this paper. The condensate dynamics is simulated with a classical-field method, using parameters that are comparable to those used in experiments [7]. The equilibrium cloud is shown in Fig. 1(b). Using simulation and analytical results for a homogeneous system, we provide insight into the reduction of the critical velocity due to the oscillating motion, the temperature, and the strong stirring potential. We derive the heating rate perturbatively in the stirring term, which shows excellent agreement with the simulations and describes the oscillating-motion broadening analytically. Furthermore, we confirm the measurements of nonzero critical velocity [7] if the superfluid response is based on the thermal fraction of the nonequilibrated cloud. We expand on this by analyzing the slow relaxation of the stirred

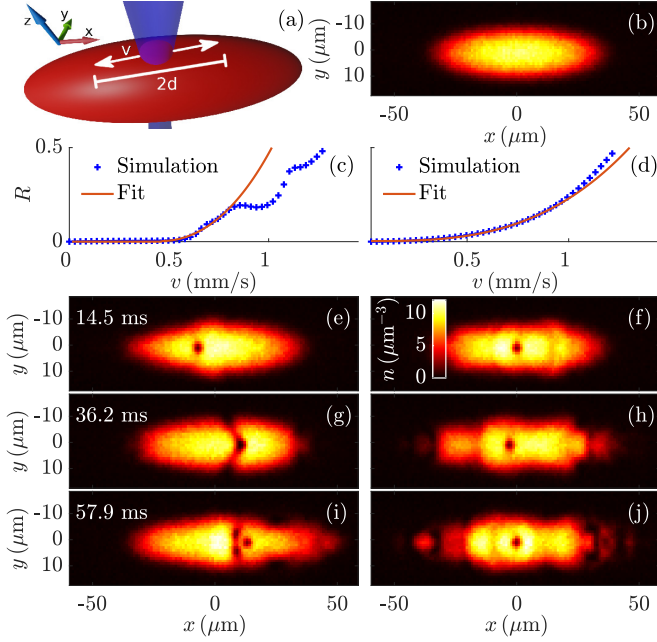


FIG. 1. (a) Sketch of the stirring process. A blue-detuned laser beam (blue) stirs a cigar-shaped cloud (red). The stirring velocity $v = 4fd$ is determined by the oscillation frequency f and the displacement d in the x direction. (b) Simulated density cloud with the density at the trap center $n_0 = 10.7 \mu\text{m}^{-3}$ and the temperature $T/T_c = 0.75$. The dimensionless heating rate R is determined as a function of v for fixed (c) $d = 20 \mu\text{m}$ and (d) $f = 56 \text{ Hz}$. The beam strength is $V_0/\mu = 2$, where μ is the mean-field energy at the trap center. The dynamics of the central plane density are shown for $v = 0.8 \text{ mm/s}$ and stirring times of (e) 14.5, (g) 36.2, and (i) 57.9 ms corresponding to (c), while the results in (f), (h), and (j) correspond to (d). The critical velocity v_c , determined via fitting (solid lines), is $0.46 \pm 0.01 \text{ mm/s}$ and 0 for the heating rate in (c) and (d), respectively.

cloud, which occurs on a timescale of 5 s much longer than the used 0.1 s relaxation time in the experiments. Finally, we discuss the dynamical regimes of phonon- and vortex-induced dissipation and show that the latter occurs for strong stirring potentials and large displacements of the stirrer.

In Figs. 1(c)–1(j) we present an example for the stirring process and the analysis of its heating rate. Given that the velocity is determined via $v = 4fd$, its magnitude can be tuned either by varying f and keeping d fixed or by varying d and keeping f fixed. The heating rate of the first scenario is shown in Fig. 1(c) and snapshots of the density distribution are shown in Figs. 1(e), 1(g), and 1(i). The heating rate of the second scenario and snapshots of the density distribution are shown in Figs. 1(d), 1(f), 1(h), and 1(j). We note that the second scenario does not give a nonzero critical velocity, determined via fitting, whereas the first scenario does. Furthermore, we note the strong excitation of the atom cloud that is visible in the snapshots, which only displays a slow relaxation to a thermalized state, as we show below. These two examples exemplify key ingredients of our subsequent discussion.

This paper is organized as follows. In Sec. II we describe our simulation method. In Sec. III we derive the analytical

heating rate and show its comparison to the simulations. In Sec. IV we detail the mechanism of vortex-induced dissipation for strong stirrers. In Sec. V we discuss the reduction of the onset of dissipation due to temperature. In Sec. VI we show the simulations for trapped clouds. In Sec. VII we describe the slow relaxation of the stirred trapped cloud. We summarize in Sec. VIII.

II. SIMULATION METHOD

Motivated by the experiments of Ref. [7], we study superfluidity of a cigar-shaped cloud of ^{23}Na atoms confined in a three-dimensional harmonic trap. We simulate the stirring dynamics using the classical-field method of Ref. [14], which builds on semiclassical-field methods such as the truncated Wigner approximation [41,42], as we describe below. The unperturbed system is described by the Hamiltonian

$$\hat{H}_0 = \int d\mathbf{r} \left[\frac{\hbar^2}{2m} \nabla \hat{\psi}^\dagger(\mathbf{r}) \cdot \nabla \hat{\psi}(\mathbf{r}) + V(\mathbf{r}) \hat{\psi}^\dagger(\mathbf{r}) \hat{\psi}(\mathbf{r}) + \frac{g}{2} \hat{\psi}^\dagger(\mathbf{r}) \hat{\psi}^\dagger(\mathbf{r}) \hat{\psi}(\mathbf{r}) \hat{\psi}(\mathbf{r}) \right], \quad (1)$$

where $\hat{\psi}$ ($\hat{\psi}^\dagger$) is the bosonic annihilation (creation) operator. The interaction constant $g = 4\pi a_s \hbar^2/m$ is determined by the s -wave scattering length a_s and the atom mass m . The external potential represents a harmonic trap $V(\mathbf{r}) = m[\omega_x^2 x^2 + \omega_\perp^2 (y^2 + z^2)]/2$, where ω_x and ω_\perp are the trap frequencies in the axial and the radial direction, respectively. To describe laser stirring we add a time-dependent term

$$\hat{H}_s(t) = \int d\mathbf{r} V(\mathbf{r}, t) \hat{n}(\mathbf{r}), \quad (2)$$

where $\hat{n}(\mathbf{r})$ is the density operator describing the density at the location $\mathbf{r} = (x, y, z)$ and $V(\mathbf{r}, t)$ is the Gaussian potential

$$V(\mathbf{r}, t) = V_0 \exp\left(-\frac{[x - x(t)]^2 + (y - y_0)^2}{2\sigma^2}\right), \quad (3)$$

which is constant in the z direction. Here V_0 is the strength and σ is the width. This potential is centered around $x(t)$ and y_0 . We set y_0 to be at the cloud center and vary $x(t)$ periodically at a constant velocity v between the points $x = -d$ and $x = d$ as described in Fig. 1(a). A constant velocity means that the velocity flips sign at the turning points instantaneously. d is chosen such that the distance between the turning points is $2d$. The potential travels a distance $4d$ during one oscillation period that is given by $T = 4d/v$. The frequency of the oscillation is $f = v/(4d)$. The periodic motion $x(t) = x(t + T)$ is described as

$$x(t) = \begin{cases} -d + vt, & 0 \leq t \leq T/2 \\ 3d - vt, & T/2 < t < T, \end{cases} \quad (4)$$

which is characterized by two parameters v and d .

For the numerical simulations we discretize space on a lattice of size $N_x \times N_y \times N_z$ and a discretization length $l = 1 \mu\text{m}$. We choose l such that it is smaller than the healing length $\xi = \hbar/\sqrt{2mgn}$ and the de Broglie wavelength $\lambda = \sqrt{2\pi\hbar^2/(mk_B T)}$ [43]. Here n is the density, T the temperature, and k_B the Boltzmann constant. In our classical-field simulation we replace the operators $\hat{\psi}$ in Eq. (1) and in the

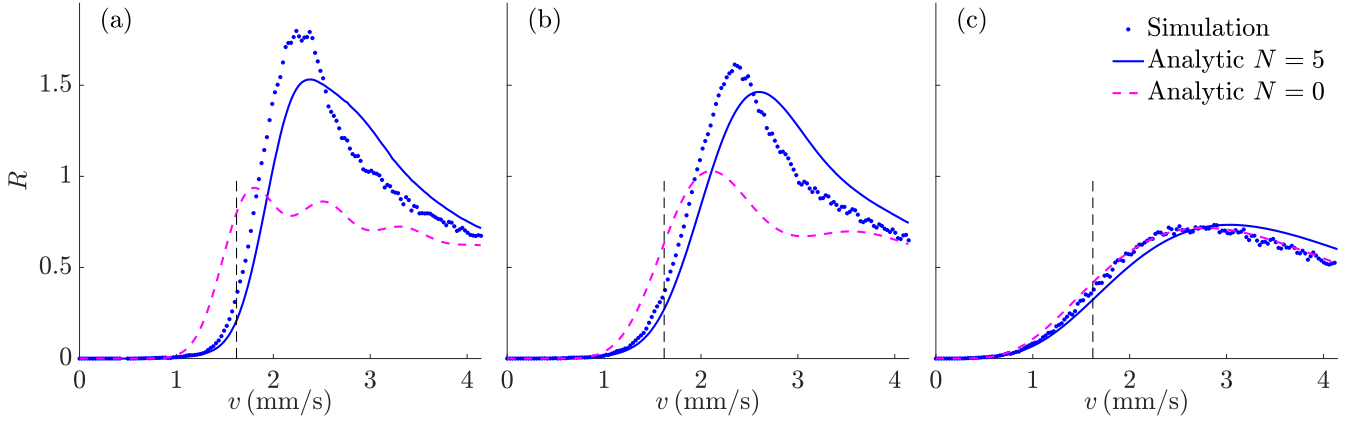


FIG. 2. Simulated heating rate R (dots) for a homogeneous condensate at $T/T_c = 0.05$, which is induced by stirring the condensate with a weak stirrer oscillating back and forth in the x direction. R is plotted as a function of the stirring velocity $v = 4fd$ for (a) $d = 20 \mu\text{m}$, (b) $d = 10 \mu\text{m}$, and (c) $d = 2.5 \mu\text{m}$. The solid lines are the Bogoliubov estimates of Eq. (12). The dashed lines correspond to Eq. (16), where the motion is approximated by a cosine stirring motion. The vertical dashed lines denote the Bogoliubov phonon velocity $v_B = 1.62 \text{ mm/s}$.

equations of motion by complex numbers ψ . We sample the initial states in a grand canonical ensemble of temperature T and chemical potential μ via a classical Metropolis algorithm. For the system parameters we choose $(\omega_x, \omega_\perp) = 2\pi \times (9, 32.5)$ Hz, the total number of atoms $N \approx 1.48 \times 10^5$, and $T/T_c = 0.75$. The critical temperature is estimated by $T_c \approx 0.94\hbar\bar{\omega}N^{1/3}/k_B$, where $\bar{\omega} = (\omega_x\omega_\perp^2)^{1/3}$ is the geometric mean of the trap frequencies [3]. This results in the trap central density $n_0 = 10.7 \mu\text{m}^{-3}$ and Thomas-Fermi diameters of 84.8 and 23.5 μm in the axial and radial directions, respectively. Since the number of atoms is one order of magnitude smaller than in the experiments, our system represents a scaled down version of the experiment. For comparison, we also consider homogeneous clouds of the average density $n = 10 \mu\text{m}^{-3}$ and various T/T_c . Here T_c is estimated as $T_c \approx 3.31\hbar^2 n^{2/3}/mk_B$ [3]. We employ a lattice of $150 \times 50 \times 50$ ($128 \times 128 \times 8$) sites for simulations of the trapped (homogeneous) cloud.

Specifically, we implement the stirring protocol as follows. We choose a set of stirring parameters V_0 , σ , d , and f . For homogeneous (trap) simulations we use $2\sigma = 2 \mu\text{m}$ (2 and 3.25 μm) and V_0 in the range $V_0/\mu = 0.08$ –5 (1–6.36). The mean-field energy $\mu = gn$ is determined using the average (maximum) density of the homogeneous (trapped) system. The stirring protocol is the following. We turn on V_0 linearly over 4 ms, stir the cloud for 72 ms, and then turn off V_0 linearly again. We repeat this for a desired set of stirring parameters and the ensemble. We calculate an ensemble average of the energy $E = \langle H_0 \rangle$ using Eq. (1), with the operators $\hat{\psi}$ replaced by complex numbers ψ . During stirring, E increases linearly with time and from its slope we determine the heating rate dE/dt , as described in detail in Appendix A 1. The dimensionless heating rate is obtained by $R = \hbar(dE/dt)/(N_{\text{cyl}}V_0^2)$, where $N_{\text{cyl}} = \pi N\sigma^2/A$ is the number of atoms in a cylinder of length L_z and radius σ , with A the system area, which is determined by $A = L_x L_y$ and $A = \pi R_x R_y$ for the homogeneous and trapped systems, respectively. Here L_x and L_y are the dimensions of the homogeneous cloud, and R_x and R_y are the Thomas-Fermi radii of the trapped condensate in the x and y directions, respectively. We show R for various system and stirring parameters below, which is typically averaged

using the initial ensemble of 100 samples. In Appendix A 2 we show the determined value of the critical velocity for a system with varying discretization lengths, which confirms that the simulation results are not affected by our choice of the discretization length.

III. HOMOGENEOUS BEC AT LOW TEMPERATURE

To understand and isolate various features of the stirring process we first consider a homogeneous condensate at a low temperature of $T/T_c = 0.05$. We stir this system with a weak stirrer following the protocol described in Sec. II. We use $V_0/\mu = 0.087$ and $2\sigma = 2.0 \mu\text{m}$. We determine the heating rate R for various values of $v = 4fd$ by varying f and keeping d constant. In Fig. 2 we show $R(v)$ for fixed $d = 20, 10$, and 2.5 μm . We find two regimes in the heating rate. For v much lower than the Bogoliubov estimate of the phonon velocity $v_B = \sqrt{gn/m} = 1.62 \text{ mm/s}$, the stirrer produces almost no heating of the system, showcasing the superfluid behavior of the condensate. For high v close to v_B , excitations are created in the system, leading to a sharp increase of the heating rate. To characterize this transition between the two regimes, we determine the onset of dissipation by a critical velocity v_c using the fitting function

$$\left(\frac{dE}{dt}\right)_{\text{fit}} = P \frac{(v^2 - v_c^2)^2}{v} + B, \quad (5)$$

with P , B , and v_c the free parameters [44]. For $R(v)$ in Fig. 2, this fitting function yields $v_c = 1.26, 1.03$, and 0.37 mm/s for $d = 20, 10$, and 2.5 μm , respectively. The magnitude of v_c is below v_B and decreases with decreasing d . We explain this below analytically.

We derive an analytical expression for the heating rate by considering the stirring term as a perturbative term [14]. We use Bogoliubov theory at zero temperature and solve the equations of motion. The total Hamiltonian of the system is $\hat{H}(t) = \hat{H}_0 + \hat{H}_s(t)$. For the unperturbed uniform system, the Bogoliubov approximation gives the diagonalized

Hamiltonian

$$\hat{H}_0 = \sum_{\mathbf{k}} \hbar\omega_{\mathbf{k}} \hat{b}_{\mathbf{k}}^{\dagger} \hat{b}_{\mathbf{k}}, \quad (6)$$

where $\hat{b}_{\mathbf{k}}$ ($\hat{b}_{\mathbf{k}}^{\dagger}$) is the Bogoliubov annihilation (creation) operator and $\hbar\omega_{\mathbf{k}} = \sqrt{\epsilon_{\mathbf{k}}(\epsilon_{\mathbf{k}} + 2mv_{\text{B}}^2)}$ is the Bogoliubov dispersion, with $\epsilon_{\mathbf{k}} = \hbar^2 k^2 / (2m)$ the free-particle dispersion. In momentum space, the stirring term becomes

$$\hat{H}_s(t) = \sum_{\mathbf{k}} V_{\mathbf{k}}(t) \hat{n}_{\mathbf{k}}, \quad (7)$$

where $V_{\mathbf{k}}(t)$ and $\hat{n}_{\mathbf{k}}$ are the Fourier transforms of the stirring potential and the density operator, respectively. To calculate $V_{\mathbf{k}}(t)$ we expand the periodic motion in Eq. (4) into a Fourier series of the form $x(t) = \sum_{\lambda=0}^N a_{\lambda} \cos(\omega_{\lambda} t)$, with a_{λ} the amplitudes and ω_{λ} the frequencies. Within the Bogoliubov approximation we use $\hat{n}_{\mathbf{k}} \approx \sqrt{N_0}(u_{\mathbf{k}} + v_{\mathbf{k}})(\hat{b}_{-\mathbf{k}}^{\dagger} + \hat{b}_{\mathbf{k}})$, where N_0 is the number of condensate atoms and $u_{\mathbf{k}}$ and $v_{\mathbf{k}}$ are the Bogoliubov parameters. This results in

$$\hat{H}_s(t) = \sum_{\mathbf{k}} V_{\mathbf{k}}(t) \sqrt{N_0}(u_{\mathbf{k}} + v_{\mathbf{k}})(\hat{b}_{-\mathbf{k}}^{\dagger} + \hat{b}_{\mathbf{k}}), \quad (8)$$

with

$$V_{\mathbf{k}}(t) = V_{\mathbf{k}} \prod_{\lambda=0}^N \exp[ik_{\lambda} a_{\lambda} \cos(\omega_{\lambda} t)]. \quad (9)$$

Here $V_{\mathbf{k}} = (2\pi V_0 \sigma^2 / A) \delta_{k_z} \exp(-k^2 \sigma^2 / 2) \exp(ik_y y_0)$ is the time-independent term. We solve the dynamical evolution created by Eqs. (6) and (8) using the ansatz

$$\hat{b}_{\mathbf{k}}(t) = e^{-i\omega_{\mathbf{k}} t} \hat{b}_{\mathbf{k}} + A_{\mathbf{k}}(t), \quad (10)$$

where $A_{\mathbf{k}}(t)$ is given by (see Appendix C)

$$A_{\mathbf{k}}(t) = -\frac{2i}{\hbar} V_{\mathbf{k}} \sqrt{N_0}(u_{\mathbf{k}} + v_{\mathbf{k}}) \sum_{v_0, \dots, v_N = -\infty}^{\infty} \prod_{\lambda=0}^N [i^{v_{\lambda}} J_{v_{\lambda}}(k_{\lambda} a_{\lambda})] \times e^{-i(\omega_{\mathbf{k}} - \omega_{\text{eff}})t/2} \frac{\sin[(\omega_{\mathbf{k}} - \omega_{\text{eff}})t/2]}{\omega_{\mathbf{k}} - \omega_{\text{eff}}}. \quad (11)$$

Here ω_{eff} is defined as $\omega_{\text{eff}} = \sum_{\lambda=0}^N v_{\lambda} \omega_{\lambda}$ and $J_{\nu}(x)$ is the Bessel function of the first kind of order ν . With Eq. (10) we determine the expectation value of the energy $\langle E(t) \rangle = \sum_{\mathbf{k}} \hbar\omega_{\mathbf{k}} \langle \hat{b}_{\mathbf{k}}^{\dagger}(t) \hat{b}_{\mathbf{k}}(t) \rangle$. This results in the energy change $\langle \Delta E(t) \rangle = \sum_{\mathbf{k}} \hbar\omega_{\mathbf{k}} |A_{\mathbf{k}}(t)|^2$. The time derivative of the energy change yields the heating rate (see Appendix C)

$$\frac{dE}{dt} = \frac{2\pi}{\hbar} \sum_{\mathbf{k}} \omega_{\mathbf{k}} (u_{\mathbf{k}} + v_{\mathbf{k}})^2 N_0 |V_{\mathbf{k}}|^2 \times \sum_{v_0, v_1, v'_1, \dots, v_N, v'_N = -\infty}^{\infty} B(k_x) \delta(\omega_{\mathbf{k}} - \omega_{\text{eff}}), \quad (12)$$

where $B(k_x)$ is given in Appendix C and includes a product of various Bessel functions of the first kind of order ν . Equation (12) cannot be reduced analytically and thus we

solve it numerically following the method described in Appendix C. To gain insight into the result in Eq. (12), we take the first-order term in the Fourier expansion $x(t) = a \cos(\omega t)$, which is a cosine motion instead of a linear oscillating motion originally considered in Eq. (4). This results in the heating rate (Appendix C)

$$\frac{dE}{dt} = \frac{2\pi}{\hbar} \sum_{\mathbf{k}, \nu} \omega_{\mathbf{k}} (u_{\mathbf{k}} + v_{\mathbf{k}})^2 N_0 |V_{\mathbf{k}}|^2 J_{\nu}^2(ak_x) \delta(\omega_{\mathbf{k}} - \nu\omega). \quad (13)$$

This expression is similar to the heating rate for a circular stirring motion in Ref. [14]. Here $a = 8d/\pi^2$ represents the one-dimensional equivalent of a radius. To solve Eq. (13) we replace the \mathbf{k} sum by an integral and obtain

$$R = 2 \sum_{\nu=-\infty}^{\infty} \tilde{k}_c^2 e^{-\tilde{k}_c^2} \frac{\sqrt{\tilde{k}_c^4 + 4\tilde{v}_{\text{B}}^2 \tilde{k}_c^2}}{\tilde{k}_c^2 + 2\tilde{v}_{\text{B}}^2} \int_0^1 d\kappa \frac{J_{\nu}^2(8\tilde{\kappa} \tilde{k}_c \tilde{d} / \pi^2)}{\sqrt{1 - \kappa^2}}, \quad (14)$$

with

$$\tilde{k}_c = (-2\tilde{v}_{\text{B}}^2 + \sqrt{4\tilde{v}_{\text{B}}^4 + \pi^2 v^2 \tilde{v}_{\text{B}}^2 \tilde{d}^2})^{1/2}. \quad (15)$$

Here $R = \hbar(dE/dt)/(N_{\text{cyl}} V_0^2)$ is the dimensionless heating rate and $\tilde{v} = v/v_{\text{B}}$, $\tilde{v}_{\text{B}} = v_{\text{B}} m \sigma / \hbar$, $\tilde{d} = d/\sigma$, and $\tilde{k} = k\sigma$ are dimensionless parameters. Equation (14) can be solved, giving

$$R = 2 \sum_{\nu=1}^{\infty} \tilde{k}_c^2 e^{-\tilde{k}_c^2} \frac{\sqrt{\tilde{k}_c^4 + 4\tilde{v}_{\text{B}}^2 \tilde{k}_c^2}}{\tilde{k}_c^2 + 2\tilde{v}_{\text{B}}^2} (8\tilde{k}_c \tilde{d} / \pi^2)^{2\nu} \Gamma^2\left(\nu + \frac{1}{2}\right) \times F\left(\nu + \frac{1}{2}, \nu + \frac{1}{2}; \nu + 1, \nu + 1, 2\nu + 1; -(8\tilde{k}_c \tilde{d} / \pi^2)^2\right), \quad (16)$$

where $F(\ell, \ell; m, m, n; x)$ is the regularized generalized hypergeometric function. We calculate the estimates of Eqs. (12) and (16) as a function of $\nu = 4fd$ for the same stirring parameters as in the simulations and show these results in Fig. 2. The results of the estimates and the simulation are consistent for $d = 2.5 \mu\text{m}$ and deviate for large d . The estimate of Eq. (12) shows a maximum at a higher ν than in the simulation. The low- ν regime of the heating rate is well captured by Eq. (12) for all d , providing an accurate estimate of the onset of dissipation, whereas the estimate of Eq. (16) captures this low- ν regime only for small d .

In Fig. 3(a) we compare the simulations of linear oscillating motion with the simulation of a linear motion. For a linear stirring motion, we choose $x(t) = vt$ moving at a constant velocity v in the $+x$ direction. We determine $R(\nu)$ and show the results in Fig. 3(a). This heating rate gives the onset of dissipation close to v_{B} . It agrees with the linear oscillating motion of $d = 20 \mu\text{m}$ for high ν and deviates for ν near v_{B} . This deviation is due to the difference between a linear oscillating motion and a linear motion, which is more pronounced for small d . For a large $d \rightarrow \infty$ our linear oscillating motion approaches a linear motion and we recover the Landau criterion of superfluidity, where v_c is approximately equal to v_{B} and dissipation above v_c occurs due to the creation of phonons. The oscillating motion results in an additional broadening of

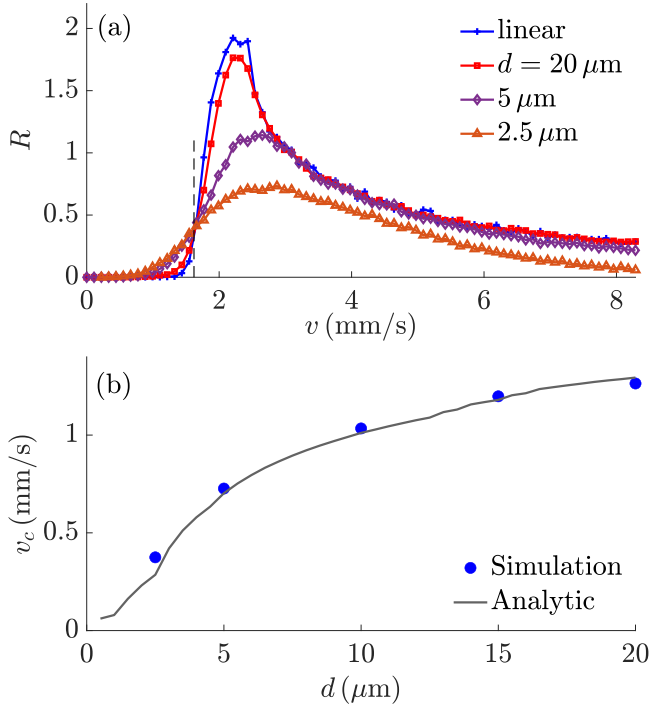


FIG. 3. (a) Simulated heating rate $R(v)$ for $d = 20, 5,$ and $2.5 \mu\text{m}$ and their comparison with the heating rate of a linear stirring motion (pluses). (b) Critical velocity v_c determined from the simulations (circles) and the Bogoliubov estimate (solid line) for various values of d .

the heating rate curve, which is responsible for an onset of dissipation at lower velocity below v_B . To quantify this reduction we determine v_c via fitting with the fitting function in Eq. (5) and present these results in Fig. 3(b). Here v_c decreases with decreasing d . We note that this reduction of v_c is similar to the reduction found for a circular stirring motion in Ref. [14], where v_c was lower for a smaller stirring radius. We compare v_c with the estimate of v_c determined using Eqs. (12) and (5). This estimate provides excellent agreement with the simulated v_c . Further, v_c appears to vanish for $d \rightarrow 0$. The

dependence of v_c on d is approximately linear for small d and sublinear for large d while approaching v_c of linear motion.

IV. STRONG STIRRING POTENTIAL

We now proceed to examine the influence of a strong stirring potential. We use the same system parameters as in Sec. III and determine the simulated heating rate $R(v)$ for various V_0 and d . In Fig. 4(a) we show $R(v)$ for $d = 20 \mu\text{m}$ and $V_0/\mu = 0.087, 0.5, 1,$ and 2 . Compared to a weak stirrer, the heating rate shows qualitative changes for a strong stirrer. The heating rate shows a steep increase at the onset of dissipation and then increases slowly with increasing v around v_B . $R(v)$ decreases at high v for all V_0 . For increasing V_0 , the onset and the maximum of the heating rate shift to a lower and a higher v , respectively. We show below that this steep onset of heating is associated with the formation of vortex-antivortex pairs. We now examine how this steep onset of heating is modified as d is reduced. In Fig. 4(b) we show $R(v)$ for $V_0/\mu = 2$ and $d = 20, 15, 10,$ and $5 \mu\text{m}$, for which the values of v are chosen below v_B . The steep onset is clearly present for $d = 20 \mu\text{m}$ as in Fig. 4(a), which is then washed out for smaller d due to increased broadening of the oscillating motion. There is no steep onset visible at all for $d = 5 \mu\text{m}$. This implies suppressed vortex-induced dissipation for small displacements. In Fig. 4(c) we show the results of v_c as a function of d for various V_0 . v_c decreases with decreasing d for all V_0 , manifesting the reduction of oscillating motion present at all V_0 . For high V_0 and large d , the reduction of v_c with respect to a weak stirrer is mainly due to the creation of vortex pairs, which we demonstrate below. For high V_0 and small d , it is due to both vortex creation and the broadening induced by the oscillating, and therefore accelerated, motion.

To investigate vortex-induced dissipation we calculate the time evolution of the phase $\phi(x, y)$ of a single plane and a single trajectory during stirring. For vortices we calculate the phase winding around the lattice plaquette of size $l \times l$ using $\sum_{\square} \delta\phi(x, y) = \delta_x\phi(x, y) + \delta_y\phi(x + l, y) + \delta_x\phi(x + l, y + l) + \delta_y\phi(x, y + l)$, where the phase difference between sites is taken to be $\delta\phi_{x,y} \in (-\pi, \pi]$. A phase winding of $+2\pi$ and -2π indicates a vortex and an antivortex, respectively.

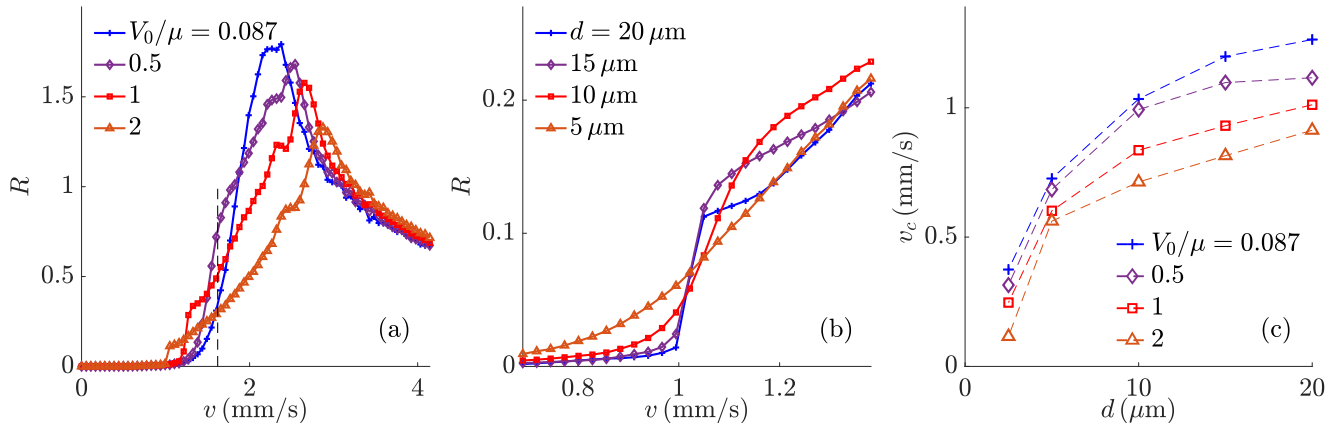


FIG. 4. (a) Plot of $R(v)$ for $d = 20 \mu\text{m}$ and $V_0/\mu = 0.087, 0.5, 1,$ and 2 . The vertical dashed line denotes the Bogoliubov velocity v_B . (b) $R(v)$ for $V_0/\mu = 2$ and different values of d . (c) v_c as a function of d for the same V_0/μ as in (a), where the dashed lines are a guide to the eye.

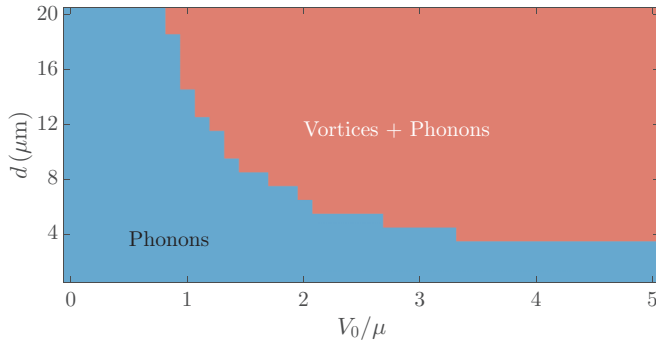


FIG. 5. Dissipation regimes as a function of V_0 and d for stirring velocity $v/v_B = 0.85$ and $T/T_c = 0.05$. The blue and the red shaded area denote the phonon and the vortex regime, respectively.

We count the total number of vortices and average it over the z direction and the ensemble. As an example, we choose a stirring velocity $v/v_B = 0.85$ and analyze the time evolution of the vortex number for various V_0 and d . If we find on average at least one vortex pair in the time evolution during stirring, we refer to this as the vortex regime. In Fig. 5 we show the dissipation regimes for vortex creation as a function of V_0 and d . For large d the onset of vortices sets in for $V_0/\mu \gtrsim 1$. This vortex region shrinks as d is reduced. For small $d < 4 \mu\text{m}$ the time evolution shows no vortex pair creation for all V_0 . This explains why a steep onset of heating is present at $d = 20, 15,$ and $10 \mu\text{m}$, and absent at $d = 5 \mu\text{m}$, for $V_0/\mu = 2$ in Fig. 4(b).

V. HIGH TEMPERATURE

Next we examine the influence of temperature. For all simulations we use the same density n as above and $V_0/\mu = 0.087$. In Fig. 6(a) we show $R(v)$ for $d = 20 \mu\text{m}$ and $T/T_c = 0.05, 0.5,$ and 0.75 . The broadening and the height of the heating rate curve increases and decreases with increasing T/T_c , respectively. This results in an onset of dissipation at low velocity for high temperature. In Fig. 6(b) we show v_c as a function of d for the same T/T_c as in Fig. 6(a). v_c decreases with both increasing T/T_c and decreasing d . While the temperature reduction is more pronounced for large d than for small d , the dependence on d is similar at both low and high temperature. This temperature reduction of v_c is due to the thermal broadening of the phonon modes and the reduction of the phonon velocity itself at nonzero temperature.

VI. TRAPPED CONDENSATE

Finally, we consider a trapped cloud as in the experiments [7]. We simulate a cigar-shaped condensate having the central density $n_0 = 10.7 \mu\text{m}^{-3}$ and $T/T_c = 0.75$. The critical temperature T_c is the estimate of a noninteracting trapped system. In all simulations we choose $d \leq 25 \mu\text{m}$ for stirring the condensate region of the cloud using the same stirring process as above. While the cloud size and the temperature are comparable to the experiments, n_0 is smaller by a factor of 10 than in the experiments to enable our numerical simulations. We first isolate the effect of oscillating motion and strength of the stirrer in the trapped cloud. We use $2\sigma = 2.0 \mu\text{m}$ and calculate

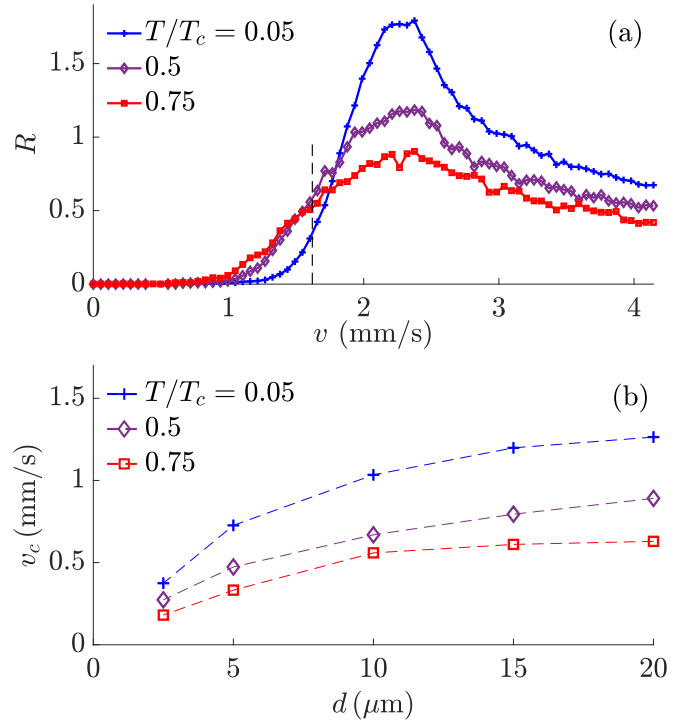


FIG. 6. (a) Plot of $R(v)$ for $d = 20 \mu\text{m}$ and $T/T_c = 0.05, 0.5,$ and 0.75 . (b) Plot of v_c as a function of d for various T/T_c as in (a).

the heating rate $R(v)$ for various d and V_0/μ . The mean-field energy $\mu = gn_0$ is determined using n_0 . In Fig. 7(a) we show $R(v)$ for $d = 20 \mu\text{m}$ and $V_0/\mu = 1, 2,$ and 5 . This heating rate shows a behavior that is similar to the case of a homogeneous system at low temperature in Fig. 3(a). Here the strong stirrer response is broadened by the thermal broadening of the phonon modes and the inhomogeneous density of the cloud. The onset of heating has contributions of vortex excitations as we demonstrate below. This vortex-induced dissipation is suppressed for small d due to increased broadening of the oscillation motion as in Fig. 7(b). In Fig. 7(c) we show v_c and its dependence on V_0 and d . In this strong stirrer regime $V_0/\mu \gtrsim 1$, v_c decreases with both increasing V_0 and decreasing d . This is similar to the case of a homogeneous system and low temperature. For large d the reduction in v_c is due to the creation of vortices that occurs at a lower velocity. This vortex creation is suppressed for small d due to increased broadening of the oscillating motion. We compare the results of v_c with the Bogoliubov estimate of the sound velocity in a cigar-shaped cloud. A sound wave in the axial direction propagates with velocity $v_B = \sqrt{gn_{\text{eff}}/m}$ near the trap center. The effective density $n_{\text{eff}} = n_0/2$ is determined by averaging the Thomas-Fermi profile in the radial direction [45]. This results in $v_{B,0} = 1.18 \text{ mm/s}$ at the trap center and $v_{B,d=20 \mu\text{m}} = 1.0 \text{ mm/s}$ at $d = 20 \mu\text{m}$. The values of v_c for $d = 20 \mu\text{m}$ are in the range $0.45\text{--}0.55 \text{ mm/s}$, which are approximately half of $v_{B,d=20 \mu\text{m}}$. This reduction of v_c is due to increased thermal fluctuations and the creation of vortices as we show below.

To understand the role of vortices in the onset of heating we analyze the time evolution of the phase $\phi(x, y)$ of the central plane of a single trajectory belonging to the same system as above. We choose the stirring velocity $v = 1.1 \text{ mm/s}$,

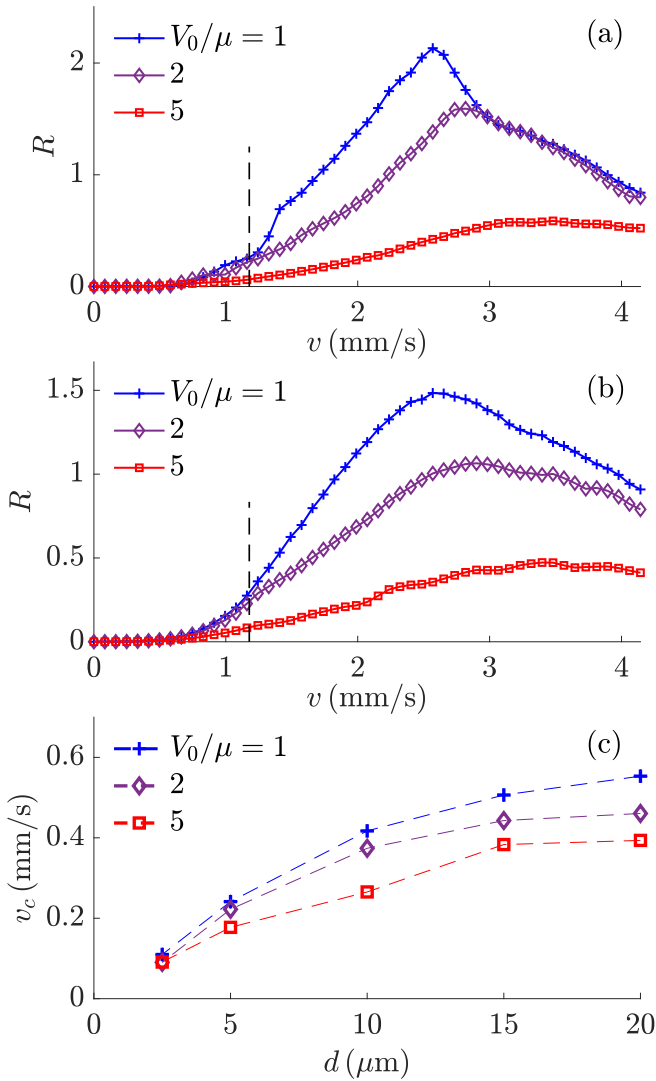


FIG. 7. (a) Simulated heating rate $R(v)$ of the trapped cloud for $d = 20 \mu\text{m}$ and $V_0/\mu = 1, 2$, and 5 . (b) Plot of $R(v)$ for $d = 5 \mu\text{m}$ and the same V_0/μ as in (a). (c) Plot of v_c as a function of d for the same V_0/μ as in (a). The vertical dashed line in (a) and (b) denotes the Bogoliubov velocity $v_{B,0}$ (see the text for details).

$V_0/\mu = 2$, and the same 2σ as above. In Figs. 8(a)–8(d) we show $\phi(x, y)$ for $d = 20 \mu\text{m}$ at the stirring time t of 14.5, 36.2, 57.9, and 72.4 ms. For $t = 14.5$ ms the phase is weakly fluctuating in the condensate cloud, indicating global phase coherence of the system. The stirring motion induces fluctuations of the phase of the system. For long stirring times these phase fluctuations are increased and result in the creation of vortex pairs. This is confirmed by the calculation of the phase winding around each plaquette, following the method described in Sec. IV. The resulting phase windings are shown in Fig. 8. Since the phase fluctuates strongly in the thermal cloud we observe a vortex plasma outside the Thomas-Fermi region. For $t = 14.5$ ms the stirring process creates no vortex pairs in the condensate region. For $t = 36.2$ ms and longer times, vortex pairs are nucleated from the regions of low density near the stirrer. In addition to this vortex shedding, vortex pairs in the thermal cloud travel to low-density regions

of the condensate cloud. In Figs. 8(e)–8(h) we show the time evolution of the phase and vortices for $d = 5 \mu\text{m}$. The vortex shedding mechanism is suppressed as no vortex creation is observed near the stirrer. Vortex pairs in the thermal cloud travel to the condensate, which is similar to the case at $d = 20 \mu\text{m}$.

To compare the simulations with the experiments [7], we follow the experimental method of stirring, which includes varying d and keeping f fixed for determining the stirring velocity $v = 4fd$. This differs from our method employed above, where we keep d fixed and vary f to determine v . We choose $V_0/\mu = 6.36$ and $2\sigma = 3.25 \mu\text{m}$, which are comparable to the experiments. In Fig. 9(a) we show R as a function of d for $f = 56, 83$, and 167 Hz. $R(d)$ shows a frequency-dependent behavior as expected. We show this result as a function of $v = 4fd$ in Fig. 9(b). The different frequency results approximately collapse at low velocities, while they differ at intermediate and high velocities. $R(v)$ is not suppressed at low velocities and increases continuously with increasing v . This results in a vanishing $v_c = 0$ for the results in Fig. 9(b). The reason for this vanishing v_c is the broadening induced by the oscillating motion, which results in a different velocity dependence in Figs. 9(b) and 9(c). The low-velocity regime $v < v_{B,0}$ includes stronger contributions of this broadening for v , or equivalently d , approaching 0. This vanishing v_c for the parameters comparable to those of the experiment is in disagreement with the measurement of a nonzero v_c [7]. As we show below, a nonzero v_c occurs in a nonequilibrium cloud which is used in the experiments, providing consistent results with the experiments. To rule out a strong stirrer effect, we calculate the heating rate for a weak stirrer of $V_0/\mu = 0.2$ and various f . We show these results in Fig. 9(c). Here $R(v)$ increases continuously with increasing v for the same f as in Fig. 9(b) and hence the critical velocity is zero. In this weak stirrer regime we recover the maximum of the heating rate, which was broadened by strong V_0 in Fig. 9(b). We also show $R(v)$ determined at a lower frequency of $f = 14$ Hz and $V_0/\mu = 0.2$ in Fig. 9(c). This result shows suppressed heating at low velocities since the oscillating motion includes larger d and the resulting broadening is reduced. This yields a critical velocity of $v_c = 0.32$ mm/s, contrary to the results of high f in Figs. 9(b) and 9(c).

To understand the observation of a nonzero v_c in the experiment, we expand on our analysis for determining v_c from the thermal fraction of the stirred cloud rather than the analysis based on the total energy $E = \langle H_0 \rangle$, as up to now. The measured v_c is determined by analyzing the thermal fraction $(1 - N_0/N)$ as a function of the stirring velocity $v = 4fd$. We extract the condensate fraction N_0/N from the central region of the *in situ* density profile after $t_{\text{relax}} = 100$ ms relaxation time, such as in Fig. 10(b), via fitting it with a Thomas-Fermi profile. This also enables us to determine the relative temperature T/T_c via $T/T_c = (1 - N_0/N)^{1/3}$ [3]. In Fig. 10(a) we show the thermal fraction as a function of v for $f = 56$ Hz and various relaxation times in the range $t_{\text{relax}} = 100$ –5000 ms. The results show a dependence on the relaxation time, implying that the system is not relaxed at short t_{relax} as in the experiment. For $t_{\text{relax}} = 100$ ms, the thermal fraction response is similar to the measurements and yields a critical velocity of $v_c = 0.73 \pm 0.44$ mm/s. The high uncertainty of v_c is a consequence of the nonequilibrium behavior of the stirred

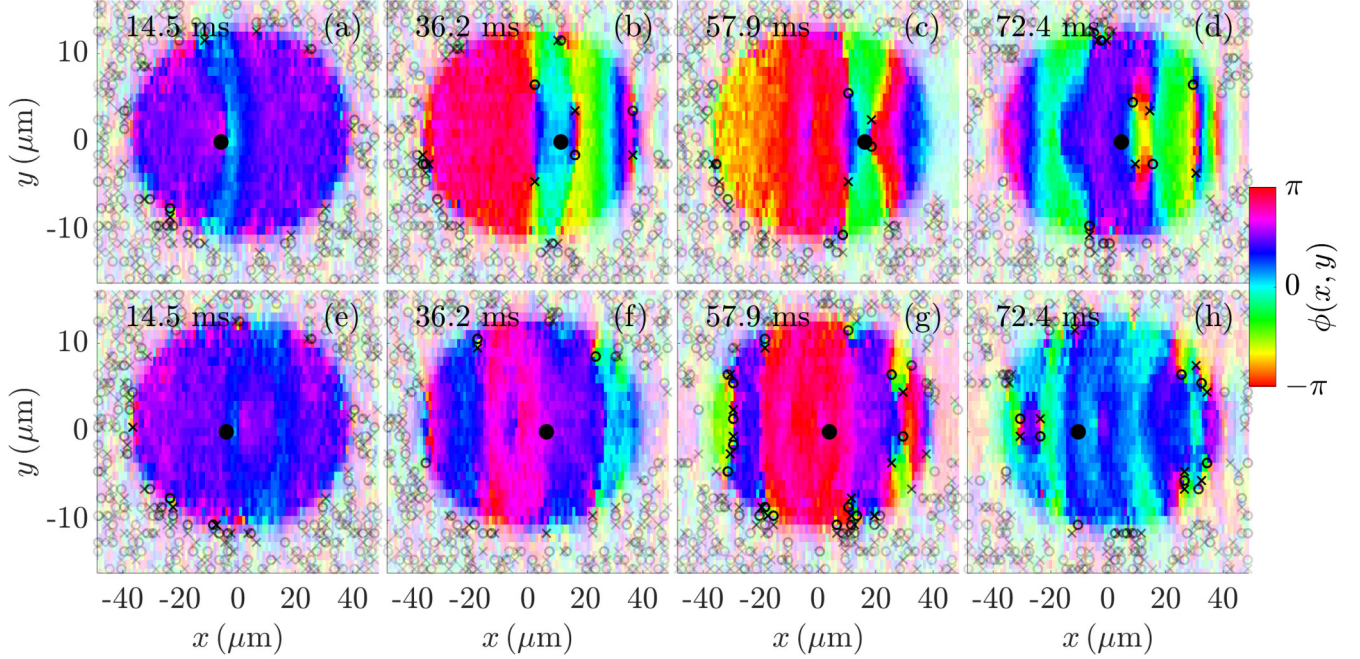


FIG. 8. Time evolution of the phase $\phi(x, y)$ of the central plane of a single trajectory during stirring at $v = 1.1$ mm/s and the stirring times $t = 14.5, 36.2, 57.9,$ and 72.4 ms for (a)–(d) $d = 20$ μm and (e)–(h) $d = 5$ μm . The circles and the crosses represent vortices and antivortices, respectively. The black disk indicates the stirrer moving back and forth in the x direction. The color transparency outside the Thomas-Fermi radius is chosen according to the density of the thermal cloud.

cloud. In Fig. 10(b) we show the density distribution of the cloud after $t_{\text{relax}} = 100$ ms for $v = 0.83$ and 3.45 mm/s. Both low- and high-velocity density profiles are not equilibrated and differ substantially from a thermalized cloud, due to the excitations induced by stirring. This is confirmed by the time evolution of the extracted thermal fraction shown as a function of t_{relax} in Fig. 10(c). The thermal fraction fluctuates at short t_{relax} and then slowly relaxes to the equilibrium value for t_{relax} of about 3–5 s. We elaborate on this in Sec. VII. This slow relaxation is also reflected in the thermal fraction shown as a function of v in Fig. 10(a), where the result converges as t_{relax} approaches 3 and 5 s. In Fig. 10(a) we also show the thermal fraction obtained from the heating rate based on the total energy of the system for $f = 56$ Hz in Fig. 9(b). For this,

we numerically invert the energy change of the temperature of the equilibrium system (see also Ref. [13]). This result agrees with the thermal fraction determined after $t_{\text{relax}} = 3$ and 5 s. This confirms that the thermal fraction of the equilibrium system increases continuously at low stirring velocities and hence no critical velocity is observed, as in the case of results in Fig. 9(b).

VII. RELAXATION DYNAMICS

To understand the relaxation dynamics we analyze the time evolution of the density and the energy of the system after stirring. We use the same system and stirrer parameters as above and stir the cloud using $v = 3.45$ mm/s and $f = 56$ Hz.

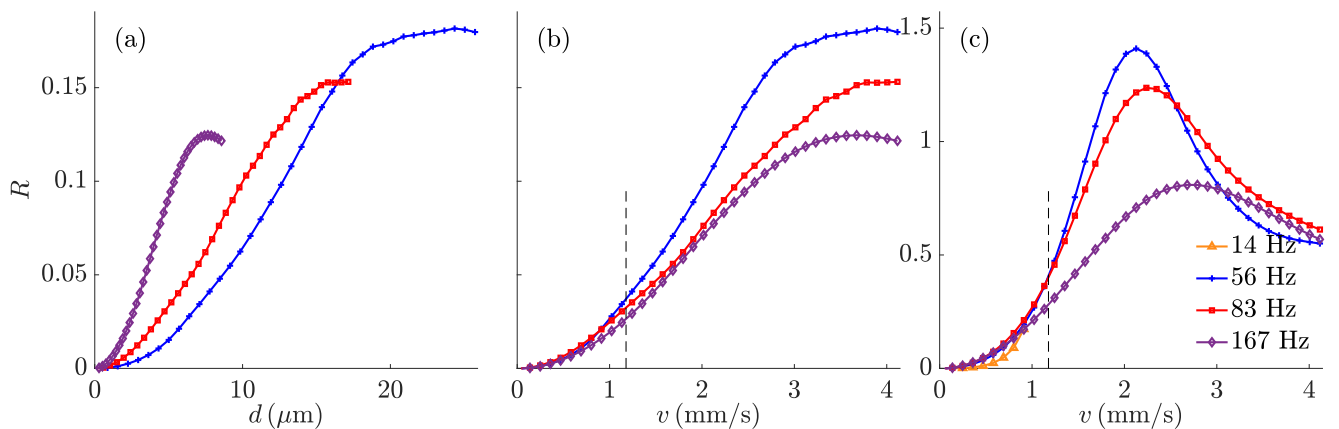


FIG. 9. (a) Plot of R as a function of d for $V_0/\mu = 6.36$ and $f = 56, 83,$ and 167 Hz. (b) $R(v)$ determined using $v = 4fd$ and the results of (a). (c) $R(v)$ for $V_0/\mu = 0.2$ and $f = 14, 56, 83,$ and 167 Hz.

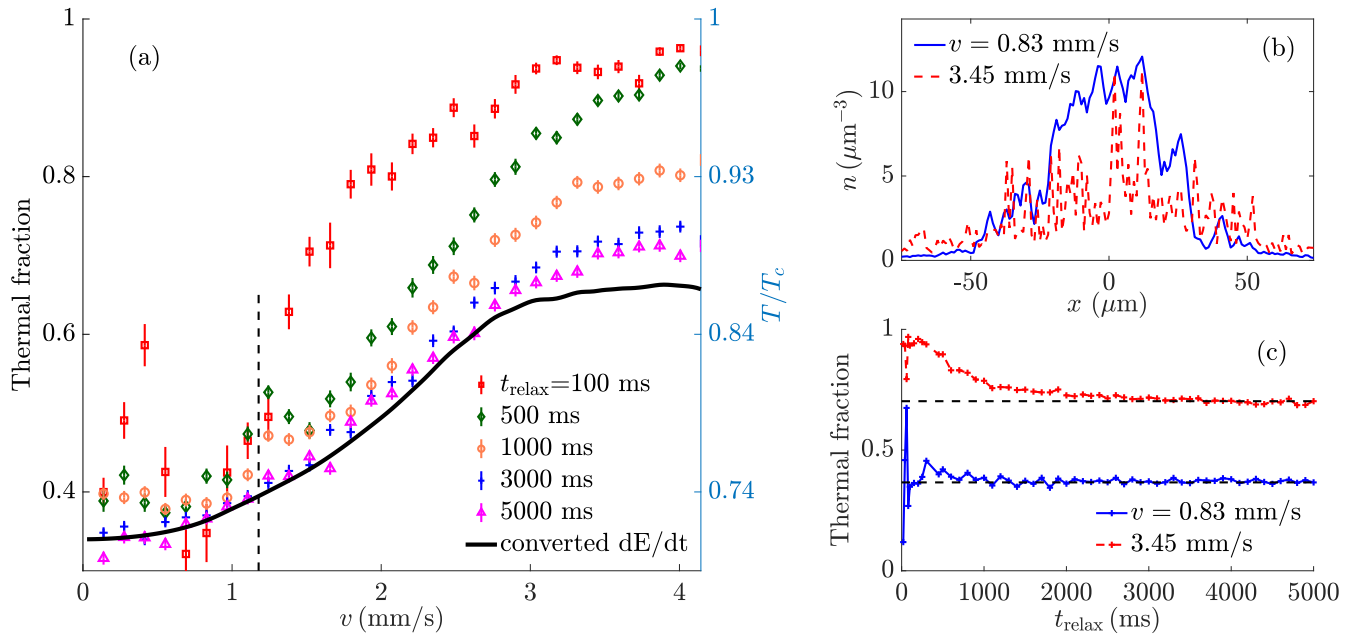


FIG. 10. (a) Thermal fraction as a function of v for various relaxation times in the range $t_{\text{relax}} = 100$ –5000 ms. The black solid line shows the thermal fraction determined from the heating rate of the system given in Fig. 9(b). (b) Density profile $n(x)$ of the cut in the x direction after $t_{\text{relax}} = 100$ ms for $v = 0.83$ and 3.45 mm/s. (c) Time evolution of the thermal fraction as a function of t_{relax} for the same v as in (b).

We calculate the density profile $n(x, y)$ of the central plane and average it over the ensemble. In Figs. 11(a)–11(d) we show the time evolution of $n(x, y)$ after stirring for $t_{\text{relax}} = 100, 500, 1000,$ and 3000 ms. For $t_{\text{relax}} = 100$ ms the density distribution shows strong fluctuations that are notably distinct

from a Thomas-Fermi profile, for this choice of the stirring parameters, which are motivated by the experiments [7]. Since the stirring potential is large and the stirring velocity is above the phonon velocity, strong depletion of the condensate region is observed for $t_{\text{relax}} = 100$ ms. The density distribution shows

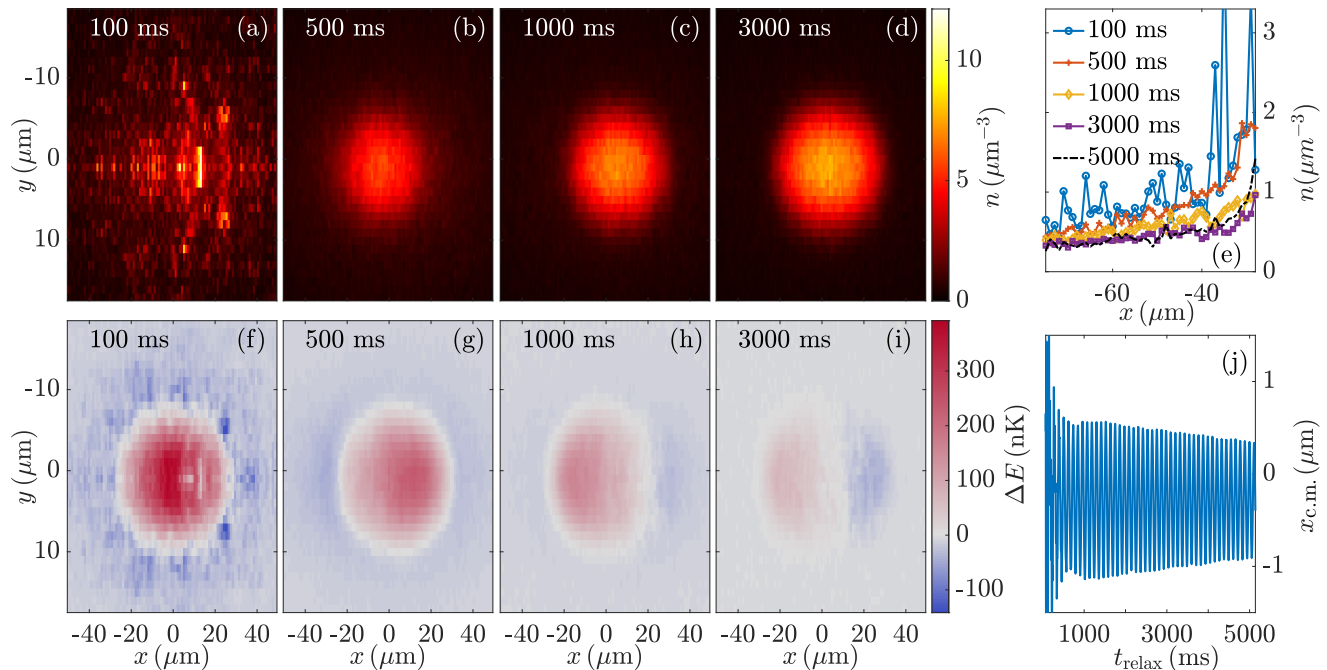


FIG. 11. Recondensation dynamics of the density profile $n(x, y)$ for the relaxation times (a) $t_{\text{relax}} = 100$, (b) $t_{\text{relax}} = 500$, (c) $t_{\text{relax}} = 1000$, and (d) $t_{\text{relax}} = 3000$ ms. The cloud was stirred using $v = 3.45$ mm/s and $f = 56$ Hz. (e) Density cut $n(x)$ in the x direction showing the thermal wing of the same cloud as in (a)–(d). Also shown is $n(x)$ of a nearly equilibrated system at $t_{\text{relax}} = 5000$ ms. (f)–(i) Time evolution of the energy difference $\Delta E(x, y) = [E_{t_{\text{relax}}}(x, y) - E_f(x, y)]/n_0$ for the same system as in (a)–(d). Here $E_{t_{\text{relax}}}(x, y)$ is the energy at time t_{relax} and $E_f(x, y)$ is the final energy of the equilibrated system. (j) Center-of-mass motion $x_{\text{c.m.}}(t)$ of the corresponding system as a function of t_{relax} .

slow recondensation dynamics and we recover a Thomas-Fermi distribution for $t_{\text{relax}} = 500$ ms. The density of the condensate region increases and finally reaches the equilibrium value for $t_{\text{relax}} \sim 3000$ ms. In Fig. 11(e) we show the thermal wing of the central cut in the x direction of the density profiles in Figs. 11(a)–11(d). The thermal wing is strongly fluctuating at short t_{relax} and then reaches the equilibrium value for $t_{\text{relax}} \sim 3$ s. We also show the result at $t_{\text{relax}} = 5$ s, which supports t_{relax} to be about 3–5 s. This slow relaxation is the origin of the higher thermal fraction than the equilibrium result in Fig. 10(a).

We now analyze the energy flow dynamics of the stirred cloud. We calculate the local energy difference per particle, i.e., $\Delta E(x, y) = [E_{t_{\text{relax}}}(x, y) - E_f(x, y)]/n_0$, where $E_{t_{\text{relax}}}(x, y)$ is the energy at time t_{relax} and $E_f(x, y)$ is the final energy of the equilibrium system. Both $E_{t_{\text{relax}}}(x, y)$ and $E_f(x, y)$ are integrated over the z direction and averaged over the ensemble. Specifically, $E(x, y)$ is obtained via

$$E(x, y) = \langle H_{\text{kin}}(x, y) \rangle + \langle H_{\text{pot}}(x, y) \rangle + \langle H_{\text{int}}(x, y) \rangle, \quad (17)$$

with

$$\langle H_{\text{kin}}(x, y) \rangle = -\frac{J}{2} \sum_{\mathbf{r}', z} \langle \psi^*(\mathbf{r})\psi(\mathbf{r}') + \psi(\mathbf{r})\psi^*(\mathbf{r}') \rangle, \quad (18)$$

$$\langle H_{\text{pot}}(x, y) \rangle = \sum_z V(\mathbf{r}) \langle |\psi(\mathbf{r})|^2 \rangle, \quad (19)$$

$$\langle H_{\text{int}}(x, y) \rangle = \frac{U}{2} \sum_z \langle |\psi(\mathbf{r})|^4 \rangle, \quad (20)$$

where \mathbf{r}' represents the neighboring sites of $\mathbf{r} = (x, y, z)$, $V(\mathbf{r})$ is the harmonic trapping potential, and $U = g/l^3$ and $J = \hbar^2/2ml^2$ are the Bose-Hubbard parameters, with l the discretization length. In Figs. 11(f)–11(i) we show $\Delta E(x, y)$ corresponding to the results presented in Figs. 11(a)–11(d). The stirred cloud reveals slow energy flow dynamics between the condensate and the thermal cloud of the system. For $t_{\text{relax}} = 100$ ms most of the stirring-induced excess energy lies within the condensate region. The system then slowly relaxes by transporting this excess energy to the thermal wings of the cloud and finally achieves equilibration for $t_{\text{relax}} \sim 3000$ ms. The energy dynamics also indicates a sloshing motion that is associated with the dipole mode of the trap, which was excited by the stirring process even though the stirring frequency was detuned above the axial trap frequency. To investigate this dipole motion we calculate the center of mass of the cloud by $x_{\text{c.m.}} = \sum_{i=1}^{N_l} n_i x_i / \sum_{i=1}^{N_l} n_i$, where N_l is the number of lattice sites and n_i is the density at site $i = (x_i, y_i, z_i)$. We average $x_{\text{c.m.}}$ over the radial direction and the ensemble. In Fig. 11(j) we show the time evolution of $x_{\text{c.m.}}(t)$ as a function of t_{relax} . Here $x_{\text{c.m.}}(t)$ oscillates at the axial trap frequency as expected. After stirring, $x_{\text{c.m.}}(t)$ shows a fast decay initially and then a slow relaxation occurring above 5 s. The energy of this dipole mode $E_{\text{c.m.}} = m\omega^2 x_{\text{c.m.}}^2/2$ is approximately 0.004 nK, which is small compared to the energy induced by the stirring process $\Delta E = 23.57$ nK. However, for low stirring velocities this energy becomes comparable to the stirring-induced energy and the relaxation of this dipole mode essentially governs the relaxation dynamics of the system. This is responsible for the

fluctuations of the thermal fraction at low stirring velocities in Fig. 10(a).

VIII. CONCLUSION

We have determined the superfluid behavior of a cigar-shaped condensate by stirring it with a repulsive Gaussian potential oscillating back and forth in the axial direction. Using both classical-field simulations and perturbation theory, we have analyzed the induced heating rate, based on the total energy of the system, as a function of the stirring velocity $v = 4fd$, where f is the frequency and d is the displacement. As the key result, we have shown that the onset of dissipation, identified via a critical velocity v_c , is influenced by the oscillating motion, the strength of the potential, the temperature, and the inhomogeneous density of the cloud. The range of these features that we studied includes the regime of large stirring potential and high temperature, which are similar to the experimental parameters of Ref. [7]. For this regime we found a vanishing critical velocity, if the heating rate was based on the total energy. In contrast to this result, we found a nonzero critical velocity if the heating rate was based on the thermal fraction of the cloud after 100 ms relaxation, which is consistent with the experimental findings. This discrepancy derives from the slow relaxation of the cloud, which is significantly out of equilibrium at 100 ms. We found that the relaxation occurs on a timescale of 5 s. Furthermore, we have mapped out the regimes of vortex- and phonon-induced dissipation and have identified a long-lived dipole oscillation contributing to the slow relaxation of the cloud.

The central points of our study are system features and phenomena in cold-atom clouds that apply to any study of superfluidity in these systems and have relevance to the studies in polariton condensates [46,47] and photonic fluids [48–50]. As such, our study supports the further exploration and understanding of superfluidity.

ACKNOWLEDGMENTS

This work was supported by the Deutsche Forschungsgemeinschaft in the framework of SFB 925 Project No. 170620586 and the excellence cluster Advanced Imaging of Matter, EXC 2056, Project No. 390715994. V.P.S. acknowledges funding from the Cluster of Excellence QuantumFrontiers, EXC 2123, Project No. 390837967.

APPENDIX A: NUMERICAL SIMULATION

1. Heating rate

In the following we elaborate on how we determine the simulated heating rate R from the induced energy change during stirring. As an example, we consider the same system and stirrer parameters as in Fig. 2(b), i.e., a homogeneous cloud at low temperature $T/T_c = 0.05$ is stirred with a weak stirrer of strength $V_0/\mu = 0.087$ and displacement $d = 10 \mu\text{m}$. In Fig. 12(a) we show the time evolution of the energy change $\Delta E(t)$ during the stirring process at the stirring velocity of $v/v_c = 0.5$. Here $\Delta E = E_f - E_i$ is the difference between the initial energy E_i and the final energy E_f of the system. In particular,

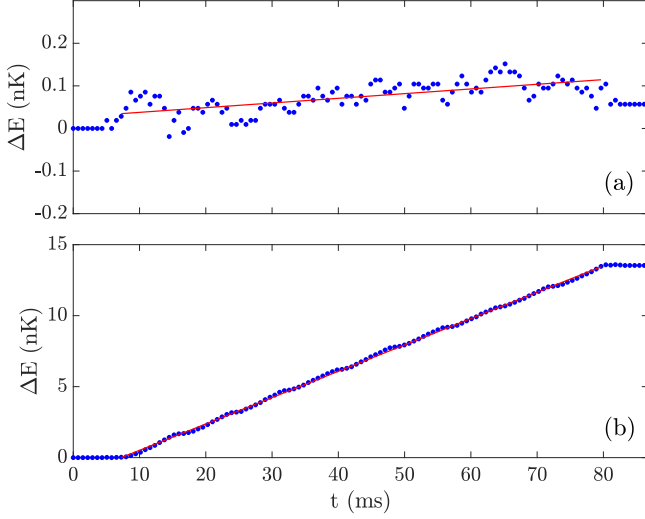


FIG. 12. Time evolution of the induced energy change $\Delta E(t)$ during the stirring process for a homogeneous cloud and stirring with a weak stirring potential. The stirring velocity (a) $v/v_c = 0.5$, where v_c is the critical velocity for the onset of dissipation, and (b) $v/v_c = 1.5$. The linear increase of the energy change is determined using a linear fit (solid line) (see the text for details).

we determine $E_{i,f}$ by $E = -(J/2) \sum_{\langle ij \rangle} (\psi_i^* \psi_j + \psi_i \psi_j^*) + (U/2) \sum_i |\psi_i|^4 + \sum_i V_i |\psi_i|^2$, which is averaged over the initial ensemble. Here ψ_i is the complex field at site i and the trapping potential is set to $V_i = 0$ for the homogeneous system. In addition, J and U are the tunneling and on-site interaction energy, respectively (see Sec. VII). The value of the critical velocity v_c is based on the results shown in Fig. 2(b). $\Delta E(t)$ increases linearly during stirring and we fit this linear increase with the function $f(t) = a + bt$ to determine the heating rate $dE/dt = b$. For $v/v_c = 0.5$ we obtain the dimensionless heating rate $R = 0.006$ (see Sec. II for the definition of R). The value of R is small, as it is expected for stirring below v_c . In Fig. 12(b) we show $\Delta E(t)$ for the stirring velocity at $v/v_c = 1.5$. This results in $R = 1.537$, which is large compared to the heating rate below v_c in Fig. 12(a). We note that on top of a global linear increase of the energy change there are small-amplitude oscillations, which come from the direction change of the stirrer when the stirrer completes the $2d$ displacement and returns. These oscillations are averaged out by our linear fitting function and hence a global heating rate R is determined.

2. Discretization length

In this section we demonstrate that the simulation results are not affected by the choice of discretization length of the numerical lattice. For this, we vary the discretization length l_{dis}/l in the range 0.5–1.5, which constitutes a change by a factor of 3. The value $l = 1 \mu\text{m}$ is the discretization length that was used for our simulations in this work. We consider the same system and stirrer parameters as in Fig. 2(b). We simulate systems with various l_{dis}/l and stir them with a weak stirrer, where the system and stirrer parameters are chosen to be the same for all systems. From the induced heating

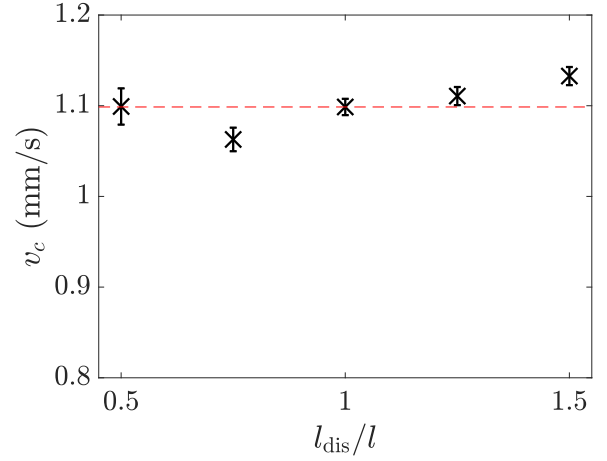


FIG. 13. Critical velocity v_c as a function of the discretization length l_{dis}/l for $n \approx 10 \mu\text{m}^{-3}$ and $T/T_c \approx 0.05$. The discretization length $l = 1 \mu\text{m}$ is used throughout the paper and the corresponding result is shown as a horizontal line.

rate we determine the critical velocity v_c , which is the main observable of our study. In Fig. 13 we show v_c as a function of l_{dis}/l . The different l_{dis}/l results fluctuate within an uncertainty of 2% and hence give a consistent critical velocity within numerical uncertainty of the simulation. This confirms that the simulation results are robust and not affected by the choice of the discretization length.

APPENDIX B: BOGOLIUBOV THEORY OF THE BOSE GAS

Within second quantization the Hamiltonian of a weakly interacting Bose gas in momentum space is given by

$$\hat{H}_0 = \sum_{\mathbf{k}} \epsilon_k \hat{a}_{\mathbf{k}}^\dagger \hat{a}_{\mathbf{k}} + \frac{g}{2V} \sum_{\mathbf{k}, \mathbf{p}, \mathbf{q}} \hat{a}_{\mathbf{k}+\mathbf{p}}^\dagger \hat{a}_{\mathbf{q}-\mathbf{p}}^\dagger \hat{a}_{\mathbf{q}} \hat{a}_{\mathbf{k}}, \quad (\text{B1})$$

where V is the volume and $\epsilon_k = \frac{\hbar^2 k^2}{2m}$. At $T = 0$ we assume macroscopic occupation of the ground state. Then we diagonalize this Hamiltonian with a Bogoliubov transformation $\hat{b}_{\mathbf{k}} = u_{\mathbf{k}} \hat{a}_{\mathbf{k}} - v_{\mathbf{k}} \hat{a}_{-\mathbf{k}}^\dagger$, where $u_{\mathbf{k}}^2 = (\hbar\omega_{\mathbf{k}} + \epsilon_{\mathbf{k}} + gn)/2\hbar\omega_{\mathbf{k}}$ and $v_{\mathbf{k}}^2 = (-\hbar\omega_{\mathbf{k}} + \epsilon_{\mathbf{k}} + gn)/2\hbar\omega_{\mathbf{k}}$. The diagonalized Hamiltonian is approximately

$$\hat{H}_0 = \sum_{\mathbf{k}} \hbar\omega_{\mathbf{k}} \hat{b}_{\mathbf{k}}^\dagger \hat{b}_{\mathbf{k}}, \quad (\text{B2})$$

where $\hbar\omega_{\mathbf{k}} = \sqrt{\epsilon_{\mathbf{k}}(\epsilon_{\mathbf{k}} + 2m v_B^2)}$.

APPENDIX C: ANALYTIC HEATING RATE

Let us expand the periodic motion into a Fourier series of the form

$$x(t) = \sum_{\lambda=0}^N a_{\lambda} \cos(\omega_{\lambda} t). \quad (\text{C1})$$

We write the Fourier transform of the stirring potential as

$$V_{\mathbf{k}}(t) = V_{\mathbf{k}} \prod_{\lambda=0}^N e^{i[k_x a_{\lambda} \cos(\omega_{\lambda} t)]}, \quad (\text{C2})$$

where $V_{\mathbf{k}} = \frac{2\pi V_0 \sigma^2}{A} \delta_{k_z} e^{-k^2 \sigma^2 / 2} e^{i k_y y_0}$ is a time-independent prefactor. We substitute $\mathcal{A}_{\mathbf{k}} = -\frac{i}{\hbar} (u_{\mathbf{k}} + v_{\mathbf{k}}) \sqrt{N_0}$ to write the equation of motion in the simple form

$$\partial_t \mathcal{A}_{\mathbf{k}}(t) = V_{\mathbf{k}} \mathcal{A}_{\mathbf{k}} e^{-i\omega_{\mathbf{k}} t} \prod_{\lambda=0}^N e^{i[k_x a_{\lambda} \cos(\omega_{\lambda} t)]}. \quad (\text{C3})$$

To integrate this expression we first use the Jacobi-Anger expansion

$$e^{i[k_x a_{\lambda} \cos(\omega_{\lambda} t)]} = \sum_{\nu=-\infty}^{\infty} i^{\nu} J_{\nu}(k_x a_{\lambda}) e^{i\nu \omega_{\lambda} t} \quad (\text{C4})$$

to get

$$\partial_t \mathcal{A}_{\mathbf{k}}(t) = V_{\mathbf{k}} \mathcal{A}_{\mathbf{k}} e^{-i\omega_{\mathbf{k}} t} \prod_{\lambda=0}^N \sum_{\nu=-\infty}^{\infty} i^{\nu} J_{\nu}(k_x a_{\lambda}) e^{i\nu \omega_{\lambda} t}. \quad (\text{C5})$$

To carry out the time integration we combine the exponentials

$$\begin{aligned} \partial_t \mathcal{A}_{\mathbf{k}}(t) &= V_{\mathbf{k}} \mathcal{A}_{\mathbf{k}} \sum_{\nu_0, \dots, \nu_N = -\infty}^{\infty} \prod_{\lambda=0}^N [i^{\nu_{\lambda}} J_{\nu_{\lambda}}(k_x a_{\lambda})] \\ &\times e^{i(\omega_{\text{eff}} - \omega_{\mathbf{k}})t}, \end{aligned} \quad (\text{C6})$$

where we substituted $\omega_{\text{eff}} = \sum_{\lambda=0}^N \nu_{\lambda} \omega_{\lambda}$. We employ the integral

$$\int_0^t dt e^{i(\omega_{\text{eff}} - \omega_{\mathbf{k}})t} = 2e^{-i(\omega_{\mathbf{k}} - \omega_{\text{eff}})t/2} \frac{\sin[(\omega_{\mathbf{k}} - \omega_{\text{eff}})t/2]}{\omega_{\mathbf{k}} - \omega_{\text{eff}}}. \quad (\text{C7})$$

Thus the solution for $\mathcal{A}_{\mathbf{k}}(t)$ is

$$\begin{aligned} \mathcal{A}_{\mathbf{k}}(t) &= 2V_{\mathbf{k}} \mathcal{A}_{\mathbf{k}} \sum_{\nu_0, \dots, \nu_N = -\infty}^{\infty} \prod_{\lambda=0}^N [i^{\nu_{\lambda}} J_{\nu_{\lambda}}(k_x a_{\lambda})] e^{-i(\omega_{\mathbf{k}} - \omega_{\text{eff}})t/2} \\ &\times \frac{\sin[(\omega_{\mathbf{k}} - \omega_{\text{eff}})t/2]}{\omega_{\mathbf{k}} - \omega_{\text{eff}}}. \end{aligned} \quad (\text{C8})$$

Taking the absolute square, we obtain

$$\begin{aligned} |\mathcal{A}_{\mathbf{k}}(t)|^2 &= 4|V_{\mathbf{k}}|^2 |\mathcal{A}_{\mathbf{k}}|^2 \sum_{\nu_0, \nu'_0, \dots, \nu_N, \nu'_N = -\infty}^{\infty} \prod_{\lambda=0}^N [i^{\nu_{\lambda} - \nu'_{\lambda}}] \\ &\times \prod_{\lambda=0}^N [J_{\nu_{\lambda}}(k_x a_{\lambda}) J_{\nu'_{\lambda}}(k_x a_{\lambda})] \\ &\times \frac{\sin[(\omega_{\mathbf{k}} - \omega_{\text{eff}})t/2]}{\omega_{\mathbf{k}} - \omega_{\text{eff}}} \frac{\sin[(\omega_{\mathbf{k}} - \omega'_{\text{eff}})t/2]}{\omega_{\mathbf{k}} - \omega'_{\text{eff}}}, \end{aligned} \quad (\text{C9})$$

where $\omega'_{\text{eff}} = \sum_{\lambda=0}^N \nu'_{\lambda} \omega_{\lambda}$. We approximate this expression by only considering terms with $\omega_{\text{eff}} = \omega'_{\text{eff}}$. This restriction reduces the number of summation indices by 1. We drop the sum over ν'_0 and write $\nu'_0 = \nu_0 + \sum_{\xi=1}^N (1 + 2\xi)(\nu_{\xi} - \nu'_{\xi})$. Thus

we get

$$\begin{aligned} |\mathcal{A}_{\mathbf{k}}(t)|^2 &= 4|V_{\mathbf{k}}|^2 |\mathcal{A}_{\mathbf{k}}|^2 \sum_{\nu_0, \nu_1, \nu'_1, \dots, \nu_N, \nu'_N = -\infty}^{\infty} (-1)^{\sum_{m=1}^N m(\nu_m - \nu'_m)} \\ &\times J_{\nu_0}(k_x a_0) J_{\nu_0 + \sum_{\xi=1}^N (1 + 2\xi)(\nu_{\xi} - \nu'_{\xi})}(k_x a_0) \\ &\times \prod_{\lambda=1}^N [J_{\nu_{\lambda}}(k_x a_{\lambda}) J_{\nu'_{\lambda}}(k_x a_{\lambda})] \frac{\sin^2[(\omega_{\mathbf{k}} - \omega_{\text{eff}})t/2]}{(\omega_{\mathbf{k}} - \omega_{\text{eff}})^2}. \end{aligned} \quad (\text{C10})$$

We define the function

$$\begin{aligned} B(k_x) &= J_{\nu_0}(k_x a_0) J_{\nu_0 + \sum_{\xi=1}^N (1 + 2\xi)(\nu_{\xi} - \nu'_{\xi})}(k_x a_0) \\ &\times \prod_{m=1}^N (-1)^{m(\nu_m - \nu'_m)} J_{\nu_m}(k_x a_m) J_{\nu'_m}(k_x a_m) \end{aligned} \quad (\text{C11})$$

and write the energy change in the system as

$$\begin{aligned} \langle \Delta E(t) \rangle &= \sum_{\mathbf{k}} \hbar \omega_{\mathbf{k}} 4|V_{\mathbf{k}}|^2 |\mathcal{A}_{\mathbf{k}}|^2 \\ &\times \sum_{\nu_0, \nu_1, \nu'_1, \dots, \nu_N, \nu'_N = -\infty}^{\infty} B(k_x) \frac{\sin^2[(\omega_{\mathbf{k}} - \omega_{\text{eff}})t/2]}{(\omega_{\mathbf{k}} - \omega_{\text{eff}})^2}. \end{aligned} \quad (\text{C12})$$

Using the approximation $\frac{\sin(\alpha t/2)}{\alpha^2} = \frac{\pi}{2} t \delta(\alpha)$, we obtain an expression for the heating rate

$$\begin{aligned} \frac{dE}{dt} &= \sum_{\mathbf{k}} 2\pi \hbar \omega_{\mathbf{k}} |V_{\mathbf{k}}|^2 |\mathcal{A}_{\mathbf{k}}|^2 \\ &\times \sum_{\nu_0, \nu_1, \nu'_1, \dots, \nu_N, \nu'_N = -\infty}^{\infty} B(k_x) \delta(\omega_{\mathbf{k}} - \omega_{\text{eff}}). \end{aligned} \quad (\text{C13})$$

We convert the sum to an integral $\sum_{k_x, k_y} = \frac{A}{(2\pi)^2} \int dk_x dk_y$, where A is the area ($x-y$ plane) of the system. Furthermore, we simplify $2\pi \hbar \omega_{\mathbf{k}} |V_{\mathbf{k}}|^2 |\mathcal{A}_{\mathbf{k}}|^2 = \frac{4\pi^3 V_0^2 \sigma^4 N_0}{m A^2} \delta_{k_z} k^2 e^{-k^2 \sigma^2}$, where we used $(u_{\mathbf{k}} + v_{\mathbf{k}})^2 \omega_{\mathbf{k}} = \frac{\hbar k^2}{2m}$. Thus we are left with

$$\begin{aligned} R &= \frac{\hbar \sigma^2}{m} \int dk_x dk_y k^2 e^{-k^2 \sigma^2} \\ &\times \sum_{\nu_0, \nu_1, \nu'_1, \dots, \nu_N, \nu'_N = -\infty}^{\infty} B(k_x) \delta(\omega_{\mathbf{k}} - \omega_{\text{eff}}). \end{aligned} \quad (\text{C14})$$

We choose to scale the heating rate as $R = \hbar \frac{dE}{dt} / (V_0^2 N_{\text{cyl}})$, where $N_{\text{cyl}} = \pi N \sigma^2 / A$. The Bogoliubov spectrum is $\omega_{\mathbf{k}} = \hbar^{-1} \sqrt{\frac{\hbar^2 k^2}{2m} (\frac{\hbar^2 k^2}{2m} + 2m v_B^2)}$, where v_B is the sound velocity. To simplify the following calculation we define $\tilde{v}_B = v_B m \sigma / \hbar$, $\tilde{k}_i = k_i \sigma$, and $\tilde{\omega}_i = \omega_i \frac{m \sigma^2}{\hbar}$ as dimensionless quantities. Thus the scaled heating rate is

$$R = \int d\tilde{k}_x d\tilde{k}_y \tilde{k}^2 e^{-\tilde{k}^2} \sum_{\nu_0, \nu_1, \nu'_1, \dots, \nu_N, \nu'_N = -\infty}^{\infty} B\left(\frac{\tilde{k}_x}{\sigma}\right) \delta(\tilde{\omega}_{\mathbf{k}} - \tilde{\omega}_{\text{eff}}), \quad (\text{C15})$$

where we used a property of the delta distribution $\delta(\frac{\hbar}{m\sigma^2}(\tilde{\omega}_k - \tilde{\omega}_{\text{eff}})) = \frac{m\sigma^2}{\hbar} \delta(\tilde{\omega}_k - \tilde{\omega}_{\text{eff}})$. In these units $\tilde{\omega}_k = \sqrt{\frac{\tilde{k}_x^2}{2}(\frac{\tilde{k}_x^2}{2} + 2\tilde{v}_B^2)}$, $\tilde{\omega}_{\text{eff}} = \sum_{\lambda=0}^N \nu_\lambda \tilde{\omega}_\lambda$, and $\tilde{\omega}_\lambda = \frac{m\sigma^2}{\hbar} \omega_\lambda$.

The zeros of the δ function lie at

$$\tilde{k}_c^2 = -2\tilde{v}_B^2 + \sqrt{4\tilde{v}_B^4 + 4\tilde{\omega}_{\text{eff}}^2}. \quad (\text{C16})$$

We use the δ function to solve the \tilde{k}_y integral. The zeros are at

$$\tilde{k}_{y,0} = (-2\tilde{v}_B^2 - \tilde{k}_x^2 + \sqrt{4\tilde{v}_B^4 + 4\tilde{\omega}_{\text{eff}}^2})^{1/2}. \quad (\text{C17})$$

Using the property $\delta(f(x)) = \frac{\delta(x-x_0)}{|f'(x_0)|}$ and the identity $\tilde{k}_c^2 = \tilde{k}_x^2 + \tilde{k}_{y,0}^2$, we obtain

$$R = \sum_{\nu_0, \nu_1, \nu'_1, \dots, \nu_N, \nu'_N = -\infty} \tilde{k}_c^2 e^{-\tilde{k}_c^2} \int_{-\tilde{k}_c}^{\tilde{k}_c} d\tilde{k}_x B\left(\frac{\tilde{k}_x}{\sigma}\right) \left(\frac{\partial \tilde{\omega}_k}{\partial k_y} \Big|_{\tilde{k}_y = \tilde{k}_{y,0}}\right)^{-1}. \quad (\text{C18})$$

Finally, we solve the derivative and substitute $\kappa = \frac{\tilde{k}_x}{\tilde{k}_c}$ to get

$$R = \sum_{\nu_0, \nu_1, \nu'_1, \dots, \nu_N, \nu'_N = -\infty} \tilde{k}_c^2 e^{-\tilde{k}_c^2} \frac{\sqrt{\tilde{k}_c^4 + 4\tilde{v}_B^2 \tilde{k}_c^2}}{\tilde{k}_c^2 + 2\tilde{v}_B^2} \int_{-1}^1 d\kappa \frac{\tilde{B}(\tilde{k}_c \kappa)}{\sqrt{1 - \kappa^2}}, \quad (\text{C19})$$

where

$$\begin{aligned} \tilde{B}(\tilde{k}_c \kappa) &= J_{\nu_0}(\tilde{k}_c \kappa \tilde{a}_0) J_{\nu_0 + \sum_{\xi=1}^N (1+2\xi)(\nu_\xi - \nu'_\xi)}(\tilde{k}_c \kappa \tilde{a}_0) \\ &\times \prod_{m=1}^N (-1)^{m(\nu_m - \nu'_m)} J_{\nu_m}(\tilde{k}_c \kappa \tilde{a}_m) J_{\nu'_m}(\tilde{k}_c \kappa \tilde{a}_m). \end{aligned} \quad (\text{C20})$$

The integral cannot be solved analytically in general. Numerically we evaluate the expression for $N = 5$. For our stirring setup the Fourier parameters are $\tilde{a}_\lambda = \frac{8\tilde{d}}{\pi^2(1+2\lambda)^2}$ and $\tilde{\omega}_\lambda = \frac{m\sigma^2}{\hbar} (2\lambda + 1) \frac{\pi v}{2d} = (2\lambda + 1) \frac{\pi \tilde{v} \tilde{v}_B}{2d}$, where we rescaled $\tilde{d} = \frac{d}{\sigma}$ and $\tilde{v} = \frac{v}{v_B}$.

- [1] P. Kapitza, Viscosity of liquid helium below the λ -point, *Nature (London)* **141**, 74 (1938).
- [2] J. F. Allen and A. D. Misener, Flow of liquid helium II, *Nature (London)* **141**, 75 (1938).
- [3] C. J. Pethick and H. Smith, *Bose-Einstein Condensation in Dilute Gases*, 2nd ed. (Cambridge University Press, Cambridge, 2008).
- [4] D. R. Allum, P. V. E. McClintock, A. Phillips, R. M. Bowley, and W. F. Vinen, The breakdown of superfluidity in liquid ^4He : An experimental test of Landau's theory, *Philos. Trans. R. Soc. London Ser. A* **284**, 179 (1977).
- [5] C. A. M. Castelijns, K. F. Coates, A. M. Guénault, S. G. Mussett, and G. R. Pickett, Landau Critical Velocity for a Macroscopic Object Moving in Superfluid ^3B : Evidence for Gap Suppression at a Moving Surface, *Phys. Rev. Lett.* **56**, 69 (1986).
- [6] P. V. E. McClintock, Ions and the Landau critical velocity in He II, *Z. Phys. B* **98**, 429 (1995).
- [7] C. Raman, M. Köhl, R. Onofrio, D. S. Durfee, C. E. Kuklewicz, Z. Hadzibabic, and W. Ketterle, Evidence for a Critical Velocity in a Bose-Einstein Condensed Gas, *Phys. Rev. Lett.* **83**, 2502 (1999).
- [8] C. Raman, R. Onofrio, J. M. Vogels, J. R. Abo-Shaeer, and W. Ketterle, Dissipationless flow and superfluidity in gaseous Bose-Einstein condensates, *J. Low Temp. Phys.* **122**, 99 (2001).
- [9] R. Onofrio, C. Raman, J. M. Vogels, J. R. Abo-Shaeer, A. P. Chikkatur, and W. Ketterle, Observation of Superfluid Flow in a Bose-Einstein Condensed Gas, *Phys. Rev. Lett.* **85**, 2228 (2000).
- [10] P. Engels and C. Atherton, Stationary and Nonstationary Fluid Flow of a Bose-Einstein Condensate Through a Penetrable Barrier, *Phys. Rev. Lett.* **99**, 160405 (2007).
- [11] R. Desbuquois, L. Chomaz, T. Yefsah, J. Léonard, J. Beugnon, C. Weitenberg, and J. Dalibard, Superfluid behaviour of a two-dimensional Bose gas, *Nat. Phys.* **8**, 645 (2012).
- [12] W. Weimer, K. Morgener, V. P. Singh, J. Siegl, K. Hueck, N. Luick, L. Mathey, and H. Moritz, Critical Velocity in the BEC-BCS Crossover, *Phys. Rev. Lett.* **114**, 095301 (2015).
- [13] V. P. Singh, C. Weitenberg, J. Dalibard, and L. Mathey, Superfluidity and relaxation dynamics of a laser-stirred two-dimensional Bose gas, *Phys. Rev. A* **95**, 043631 (2017).
- [14] V. P. Singh, W. Weimer, K. Morgener, J. Siegl, K. Hueck, N. Luick, H. Moritz, and L. Mathey, Probing superfluidity of Bose-Einstein condensates via laser stirring, *Phys. Rev. A* **93**, 023634 (2016).
- [15] K. W. Madison, F. Chevy, W. Wohlleben, and J. Dalibard, Vortex Formation in a Stirred Bose-Einstein Condensate, *Phys. Rev. Lett.* **84**, 806 (2000).
- [16] S. Inouye, S. Gupta, T. Rosenband, A. P. Chikkatur, A. Görlitz, T. L. Gustavson, A. E. Leanhardt, D. E. Pritchard, and W. Ketterle, Observation of Vortex Phase Singularities in Bose-Einstein Condensates, *Phys. Rev. Lett.* **87**, 080402 (2001).
- [17] J. R. Abo-Shaeer, C. Raman, J. M. Vogels, and W. Ketterle, Observation of vortex lattices in Bose-Einstein condensates, *Science* **292**, 476 (2001).
- [18] M. W. Zwierlein, J. R. Abo-Shaeer, A. Schirotzek, C. H. Schunck, and W. Ketterle, Vortices and superfluidity in a strongly interacting Fermi gas, *Nature (London)* **435**, 1047 (2005).
- [19] W. J. Kwon, G. Moon, S. W. Seo, and Y. Shin, Critical velocity for vortex shedding in a Bose-Einstein condensate, *Phys. Rev. A* **91**, 053615 (2015).
- [20] W. J. Kwon, J. H. Kim, S. W. Seo, and Y. Shin, Observation of von Kármán Vortex Street in an Atomic Superfluid Gas, *Phys. Rev. Lett.* **117**, 245301 (2016).
- [21] J. W. Park, B. Ko, and Y. Shin, Critical Vortex Shedding in a Strongly Interacting Fermionic Superfluid, *Phys. Rev. Lett.* **121**, 225301 (2018).
- [22] D. E. Miller, J. K. Chin, C. A. Stan, Y. Liu, W. Setiawan, C. Sanner, and W. Ketterle, Critical Velocity for Superfluid Flow across the BEC-BCS Crossover, *Phys. Rev. Lett.* **99**, 070402 (2007).
- [23] I. Ferrier-Barbut, M. Delehaye, S. Laurent, A. T. Grier, M. Pierce, B. S. Rem, F. Chevy, and C. Salomon, A mixture of Bose and Fermi superfluids, *Science* **345**, 1035 (2014).

- [24] M. Wenzel, F. Böttcher, J.-N. Schmidt, M. Eisenmann, T. Langen, T. Pfau, and I. Ferrier-Barbut, Anisotropic Superfluid Behavior of a Dipolar Bose-Einstein Condensate, *Phys. Rev. Lett.* **121**, 030401 (2018).
- [25] L. Sobirey, N. Luick, M. Bohlen, H. Biss, H. Moritz, and T. Lompe, Observation of superfluidity in a strongly correlated two-dimensional Fermi gas, *Science* **372**, 844 (2021).
- [26] J. H. Kim, D. Hong, K. Lee, and Y. Shin, Critical Energy Dissipation in a Binary Superfluid Gas by a Moving Magnetic Obstacle, *Phys. Rev. Lett.* **127**, 095302 (2021).
- [27] G. Gauthier, M. T. Reeves, X. Yu, A. S. Bradley, M. A. Baker, T. A. Bell, H. Rubinsztein-Dunlop, M. J. Davis, and T. W. Neely, Giant vortex clusters in a two-dimensional quantum fluid, *Science* **364**, 1264 (2019).
- [28] K. E. Wilson, E. C. Samson, Z. L. Newman, and B. P. Anderson, Generation of high winding-number superfluid circulation in Bose-Einstein condensates, [arXiv:2109.12945](https://arxiv.org/abs/2109.12945).
- [29] W. J. Kwon, G. Del Pace, K. Xhani, L. Galantucci, A. Muzi Falconi, M. Inguscio, F. Scazza, and G. Roati, Sound emission and annihilations in a programmable quantum vortex collider, *Nature (London)* **600**, 64 (2021).
- [30] T. Winiecki, J. F. McCann, and C. S. Adams, Pressure Drag in Linear and Nonlinear Quantum Fluids, *Phys. Rev. Lett.* **82**, 5186 (1999).
- [31] J. S. Stieflberger and W. Zwerger, Critical velocity of superfluid flow past large obstacles in Bose-Einstein condensates, *Phys. Rev. A* **62**, 061601(R) (2000).
- [32] B. Jackson, J. F. McCann, and C. S. Adams, Dissipation and vortex creation in Bose-Einstein condensed gases, *Phys. Rev. A* **61**, 051603(R) (2000).
- [33] M. Crescimanno, C. G. Koay, R. Peterson, and R. Walsworth, Analytical estimate of the critical velocity for vortex pair creation in trapped Bose condensates, *Phys. Rev. A* **62**, 063612 (2000).
- [34] A. C. Mathey, C. W. Clark, and L. Mathey, Decay of a superfluid current of ultracold atoms in a toroidal trap, *Phys. Rev. A* **90**, 023604 (2014).
- [35] C. Feng and M. J. Davis, Superfluid critical velocity of an elongated harmonically trapped Bose-Einstein condensate, [arXiv:1909.13657](https://arxiv.org/abs/1909.13657).
- [36] C. Feng and M. J. Davis, Influence of quantum fluctuations on the superfluid critical velocity of a one-dimensional Bose gas, *Eur. Phys. J. D* **74**, 86 (2020).
- [37] V. P. Singh and L. Mathey, Collective modes and superfluidity of a two-dimensional ultracold Bose gas, *Phys. Rev. Res.* **3**, 023112 (2021).
- [38] D.-C. Zheng, Y.-Q. Yu, and R. Liao, Tuning dissipation and excitations in superfluid Fermi gases with a moving impurity, *Phys. Rev. A* **100**, 033611 (2019).
- [39] S. Jin, S. Laurent, and F. Chevy, Hydrodynamic response of a trapped superfluid to a periodic perturbation, *Eur. Phys. J.: Spec. Top.* **227**, 2263 (2019).
- [40] J. Rønning, A. Skaugen, E. Hernández-García, C. Lopez, and L. Angheluta, Classical analogies for the force acting on an impurity in a Bose-Einstein condensate, *New J. Phys.* **22**, 073018 (2020).
- [41] P. B. Blakie, A. S. Bradley, M. J. Davis, R. J. Ballagh, and C. W. Gardiner, Dynamics and statistical mechanics of ultracold Bose gases using c-field techniques, *Adv. Phys.* **57**, 363 (2008).
- [42] A. Polkovnikov, Phase space representation of quantum dynamics, *Ann. Phys. (NY)* **325**, 1790 (2010).
- [43] C. Mora and Y. Castin, Extension of Bogoliubov theory to quasicondensates, *Phys. Rev. A* **67**, 053615 (2003).
- [44] G. E. Astrakharchik and L. P. Pitaevskii, Motion of a heavy impurity through a Bose-Einstein condensate, *Phys. Rev. A* **70**, 013608 (2004).
- [45] S. Stringari, Dynamics of Bose-Einstein condensed gases in highly deformed traps, *Phys. Rev. A* **58**, 2385 (1998).
- [46] A. Amo, J. Lefrère, S. Pigeon, C. Adrados, C. Ciuti, I. Carusotto, R. Houdré, E. Giacobino, and A. Bramati, Superfluidity of polaritons in semiconductor microcavities, *Nat. Phys.* **5**, 805 (2009).
- [47] G. Lerario, A. Fieramosca, F. Barachati, D. Ballarini, K. S. Daskalakis, L. Dominici, M. De Giorgi, S. A. Maier, G. Gigli, S. Kéna-Cohen, and D. Sanvitto, Room-temperature superfluidity in a polariton condensate, *Nat. Phys.* **13**, 837 (2017).
- [48] D. Vocke, K. Wilson, F. Marino, I. Carusotto, E. M. Wright, T. Roger, B. P. Anderson, P. Öhberg, and D. Faccio, Role of geometry in the superfluid flow of nonlocal photon fluids, *Phys. Rev. A* **94**, 013849 (2016).
- [49] C. Michel, O. Boughdad, M. Albert, P.-É. Larré, and M. Bellec, Superfluid motion and drag-force cancellation in a fluid of light, *Nat. Commun.* **9**, 2108 (2018).
- [50] J. Huynh, M. Albert, and P.-É. Larré, Critical velocity for superfluidity in the one-dimensional mean-field regime: From matter to light quantum fluids, *Phys. Rev. A* **105**, 023305 (2022).